31st Congress of the International Council
of the Aeronautical Sciences

Belo Horizonte, Brazil; September 09-14, 2018

MULTI-DISCIPLINARY OPTIMISATION OF MEDIUM ALTITUDE LONG ENDURANCE UAVS

Dries Verstraete[*]
[*]**School of Aerospace, Mechanical and Mechatronic Engineering, The University of Sydney**

Keywords: *multi-disciplinary optimisation, MALE, UAV, fuel cell, piston engine*

Abstract

While electric propulsion is generally preferred for small unmanned aerial vehicles, medium altitude long endurance unmanned vehicles typically employ piston engines due to the limited energy density of batteries. Fuel cells could enable electric propulsion for medium altitude UAVs. The current article presents a multidisciplinary design and optimisation framework that allows a comparison between piston engines and fuel cells as a propulsion system for medium altitude long endurance UAVs. Models are developed for both propulsion technologies and applied to the design of a typical medium altitude long endurance. The results of the study show that fuel-cell-powered UAVs can be considerably lighter than UAVs powered by piston engines regardless of whether hydrogen fuel is stored as compressed gas or in liquid form. For a given take-off weight the use of fuel cells almost doubles the endurance of the UAV and endurances over 60 hours are achievable with take-off gross weights less than 1000 kg.

1 Introduction

Unmanned aerial vehicles (UAVs) are increasingly the platform of choice for a variety of reconnaissance and remote-sensing missions, aerial photography, environmental monitoring, disaster relief, and search and rescue operations. Small UAVs primarily use electrical propulsion systems because of their comparatively high efficiency, low cost, and high reliability [1–7], as well as low infra-red and noise levels [8]. Larger UAVs are, on the other hand, predominantly powered by piston engine or gas turbines as the energy density of current battery technology would lead to an excessive take-off gross weight for typical endurances of medium altitude long endurance (MALE) UAVs.

Fuel cells offer a considerably higher energy density than batteries [9] and could enable electric propulsion for MALE UAVs. However their integration needs to be properly addressed as fuel cell performance characteristics differ significantly from those of piston engines. Fuel cell efficiency, for instance, increases at part load [9] and the lower operating pressure at altitude can have a significant impact on fuel cell power levels [10–12]. To assess those differences properly a multi-disciplinary design environment is needed.

The current article presents a multidisciplinary design and optimisation framework that enables investigation of these integration differences. The UAV design and performance analysis framework is detailed first. After this detailed performance models for piston engines and fuel cells are described. Those models are then coupled with the UAV design framework and applied to a nominal MALE UAV design. For both propulsion technologies the UAV wing area and aspect ratio are optimised to minimise the maximum gross take-off weight of the UAV.

2 UAV Design and Performance Analysis Framework

The overall architecture of the UAV design framework is presented in Figure 1. As shown, the design is based on mission specifications. These mission specifications are used to define an initial geometry and to obtain a first estimate of the required wing size, and wing aspect ratio, as well as an initial guess for the take-off weight. Initial values are derived from a regression analysis of existing UAVs [13].

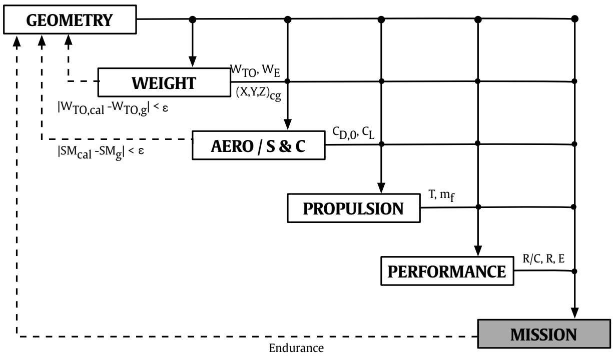

Fig. 1 Structure of the UAV design framework

The airframe geometry is used to calculate the weight of the various components, and to determine the aerodynamic performance and stability derivatives. For a given geometry, two iterations are performed. Take-off weight W_{TO} is updated until convergence, and the component position is varied to obtain the required static margin SM. After these iterations are converged, the propulsion unit is sized and the overall mission performance is calculated. If the imposed mission endurance is not reached, the geometry and take-off weight are updated, and the process is started over.

Each module of the UAV design and performance analysis is described hereafter. Mission input and modelling is detailed first, after which aerodynamic and performance calculations are outlined. Methods used to calculate component weights are reported next. As several propulsion technologies are compared in the results section, the propulsion models are detailed in the next section.

2.1 Mission

UAVs are predominantly used for surveillance and reconnaissance missions, hence a typical surveillance mission is adopted where the UAV cruises to its target area, loiters over the designated area, and cruises back to the launch point (Figure 2). The loiter phase is the main phase of the mission where the payload is turned on and the UAV is performing its surveillance task. For this mission type loiter endurance is the main input variable for the mission routine. However, cruise altitude and speed, rate-of-climb and climb speed, as well as loiter speed need to be detailed too. For the medium altitude long endurance (MALE) UAVs in this investigation a cruise altitude of 20,000 ft (6096m) is selected. Cruise (ingress and egress) speed is set at 80 kts (43.2 m/s) while a loiter and climb speed of 65 kts (35.1 m/s) are adopted. Rate-of-climb varies from 6.5 m/s at sea-level to 2.7 m/s at top-of-climb and ingress and egress distance is set to 100 nm (185.2 km) [14, 15].

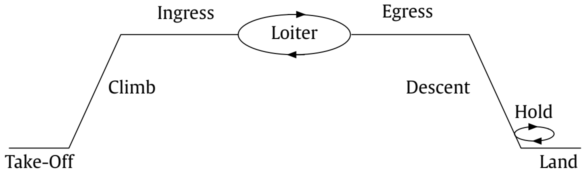

Fig. 2 Segments used in the mission profile

2.2 Aerodynamics and Performance

Aerodynamic and stability and control are calculated with the digital version of the USAF Stability and Control Data Compendium (DatCom) [16, 17]. Trimmed lift and drag data is generated for all flight conditions as input for the mission performance calculation. DatCom results are also used to calculate the static margin and a minimum static margin of 10% is imposed [18].

Performance is calculated for each mission segment (Figure 2) based on the trimmed aerodynamic data. Energy-intensive flight segments like climb, ingress, loiter, egress and descent are divided into multiple subsections for accuracy. For each energy-intensive flight segment, Breguet style equations are employed [19]. Once the total energy requirement is known the weight of the energy source and the overall aircraft take-off weight are updated.

2.3 Geometry

Throughout the design iterations fuselage size is updated to ensure that the fuselage has the necessary internal volume to store all components. The fuselage shape is based on minimum drag shapes for axisymmetric bodies [20].

Wing geometry is defined based on wing area, wing aspect ratio, and wing taper ratio. A straight-tapered wing geometry is assumed for all cases. The wing is unswept and an SD7062 airfoil is used. This airfoil was selected for its good aerodynamic performance and high lift capability at low Reynolds numbers [6].

Wing location is selected so that the aerodynamic centre of the wing is positioned at 48% of the length of the fuselage [21]. This assures a reasonable tail moment arm for sizing and ensures trimmability in DatCom.

Both the horizontal and vertical tail are sized using tail volume coefficients [18, 22–27]. The horizontal tail volume coefficient V_{ht} is set to 0.45 [18, 24–27]. As the vertical tail area strongly depends on the wing span, the vertical tail volume coefficient is linearly decreased with wing aspect ratio. Without this vertical tails become excessively large at low aspect ratios and extremely small at high aspect ratios. Based on trends for sailplane vertical tails [27], the vertical tail volume coefficient is set to 0.015 for a wing aspect ratio of 15 and decreases linearly to 0.009 at a wing aspect ratio of 25. A corresponding increase for lower aspect ratio wings is also adopted. Two constraints are imposed on the fuselage length to ensure a tail moment arm that allows trimming. The first constraint sets the minimum fuselage length as 35% of the wing span [21]. This protects the fuselage minimum length for high aspect ratio cases. The second constraint ensures that the fuselage is longer than 3 mean aerodynamic chords, which acts as a protection for low aspect ratio cases.

The horizontal tail aspect ratio is set to 4.5 for a taper ratio of 1 [18, 22–24, 27]. Vertical tail aspect ratio is taken as 1.5 with a taper ratio of 0.5 [18, 22–24, 27]. Ailerons cover 20% of the wing chord and 50% of the wing span. The elevator spans the entire horizontal tail and covers 50% of the tail area while the rudder takes up 40% of the vertical tail.

2.4 Weight Calculations

To calculate the overall take-off weight, the following breakdown is used:

$$W_{TO} = W_E + W_{PL} + W_F \tag{1}$$

where W_{TO} is the take-off weight of the aircraft, W_E is the aircraft empty weight, and W_{PL} is the weight of the payload. The mission 'fuel' weight W_F is calculated based on the mission specification and the fuel/energy consumption of the propulsion technology under consideration. The aircraft empty weight is calculated using a component weight build-up:

$$W_E = (W_{AF} + W_{sys} + W_{prop}) \cdot (1 + M_{EW}) \tag{2}$$

where W_{AF} is the airframe weight, W_{sys} is the weight of the systems and avionics, W_{prop} is the weight of the total propulsion system, and M_{EW} presents a 6% growth margin on the empty weight to account for small differences in build quality, construction, ... [18, 28, 29].

The airframe weight is split into the wing weight, fuselage weight, empennage weight, and tailboom weight. Wing weight is calculated using the physics-based methodology described in ref. [30] to accurately reflect changes in component weight with size. Three additional regression-based methods are added for improved accuracy during the optimisation runs. A method for general aviation aircraft wings was adopted from ref. [22]. The other two methods are derived from sailplane correlations given in refs. [18, 26]. The final wing weight is taken as the average of the 4 prediction methods.

Fuselage and empennage weight are calculated using the average of two regression methods [18, 31]. The weight of the systems and avionics, electrical wiring, and electrical systems is calculated based on the methods presented in refs. [18, 21]. An autopilot weight of 10 lbs is used [18], and a power consumption of 15 W per lb of system is assumed for the avionics [32]. Propeller weight is calculated using the method from refs. [18, 33]. Finally, where applicable, the weight of the brushless DC motor is determined from a regression analysis on a large database of brushless DC motors [34] while the weight of the electronic speed controller is taken as 0.04 kg/kW [18, 35].

2.5 Propeller

While a detailed sizing and optimisation of the propeller is beyond the scope of this article, the variation in propeller efficiency with flight condition can have a significant impact on the performance estimates [36]. A method is thus adopted that allows a rapid evaluation of the propeller efficiency while still providing accuracy across the entire mission. The adopted methodology is based on the so-called propeller polar [37]:

$$\frac{C_P}{J^2} = \left(m + n\frac{C_T}{J^2} \right) \tag{3}$$

where C_P represents the power coefficient of the propeller, J is the propeller advance ratio, and C_T is the thrust coefficient. Based on measured propeller performance [38] it is furthermore assumed that the thrust coefficient varies linearly with the advance ratio:

$$C_T = a + bJ \tag{4}$$

Whereas this assumption is not valid at low advance ratios, it gives an accurate approximation of the propeller performance across the expected operating range for the main flight phases. Combining the two previous equations furthermore allows a simple expression for the propeller efficiency:

$$\eta = \frac{aJ + bJ^2}{mJ^2 + nbJ + na} \tag{5}$$

This expression is used to fit data of a typical variation in normalised propeller efficiency with a normalised advance ratio [22]. The advance ratio is normalised by its value at the peak efficiency while efficiency is normalised by its peak value. Using a non-linear least squares fit on the data of ref. [22] results in the following coefficients:$a = 0.9106$; $b = -0.641$; $m = 0.06075$; $n = 0.7772$. The efficiency at the different flight conditions can be determined once the normalisation values for both advance ratio and efficiency are known. Here, peak efficiency is set to 83% while the advance ratio at which the peak efficiency occurs is, on the other hand, set at the mid-loiter point so that the propeller operates close to its peak efficiency for the most energy-demanding phase of the flight. For off-design operation the rotational speed to deliver the required thrust is calculated. The propeller diameter is determined using the method from refs. [22, 39]. The diameter is calculated for climb, ingress, egress and loiter and the maximum value of all 4 flight conditions is taken.

3 Propulsion Systems Modelling

As a comparison is made between piston engines and fuel-cell-based propulsion system, a detailed description of the modelling method adopted for both technologies is given next. Piston engine models are detailed first, while fuel cell, brushless DC motors and hydrogen storage models are subsequently described.

3.1 Piston Engines

The current section describes scaling laws and a performance model for piston engines. Scaling laws are derived from a database of 488 piston engines. Of those, 294 are two-stroke engines, and 194 use a four-stroke cycle. Entries in the database range from small hobby-market engines to large engines used on general aviation aircraft[1]. Regression dilution is avoided using the

---

[1] Manufacturers in the database include a.o. 3W, Continental, Desert Aircraft, DL Engines, Enya, Evolution Engines, Hirth, Honda, Limbach, Lycoming, Northwest UAV,

techniques described in ref. [13].

3.1.1 Engine Power and Mass

As suggested in ref. [40], engine physical and performance properties are analysed with respect to the engine displacement volume. As will be shown, this leads to good correlations and identifiable trends for all considered parameters. However, engine displacement is of little use when designing an aircraft or calculating its performance. In a first step engine displacement is therefore correlated with engine peak power and a power law regression is performed [40]:

$$V_d = AP_{eng}^B \tag{6}$$

where V_d is the total engine displacement, and P_{eng} is the engine peak power. A good correlation is obtained between peak power and total displacement (Figure 3). This is reflected by the small relative uncertainty (R.U.) on the regression fits (Table 1).

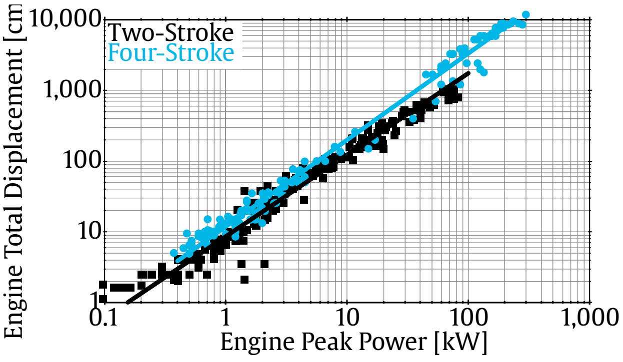

Fig. 3 Engine displacement as function of engine peak power.

A large spread exists on each of the datasets, and the data for the different engine types shows a significant overlap. The identified correlations are nonetheless statistically different, as shown by a two-sample t-test on the two datasets (performed using the MATLAB® `ttest2` function, without assuming equal variances of the datasets).

Table 1 Regression coefficients for power-law fits of engine displacement as a function of engine peak power, where V_d is in cm^3 and P in kW. 2S indicates two-stroke engines while 4S stands for four-stroke.

	A	B	R^2	R.U.
2S	8.6163	1.1540	0.9708	3.5%
4S	11.8987	1.2242	0.9847	5.2%

Note that the accuracy of the fit for two-stroke engines reduces for small engine displacements (Figure 3). For small engines, friction losses and charge leakage through the cylinder-piston gap namely become dominant [41]. Care must thus be taken when engine power is less than approximately 500 W.

With the engine displacement volume known, engine mass can be determined next. A similar power law regression analysis was performed to obtain engine mass (m_{eng}) as function of engine displacement (Figure 4 and Table 2):

$$m_{eng} = AV_d^B \tag{7}$$

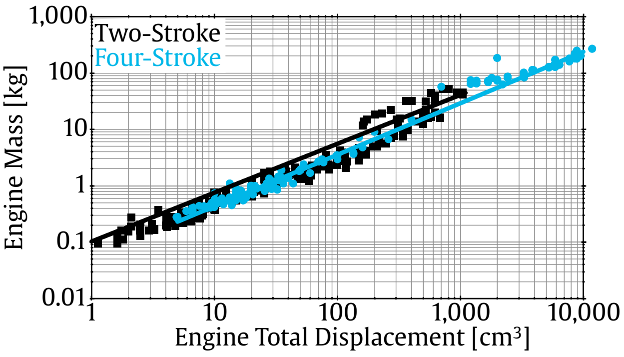

Fig. 4 Engine mass as function of engine displacement.

3.1.2 Torque and Rotational Speed

Engine rotational speed and torque need to be determined so that the engine and propeller can be matched. To allow engine scaling, a regression analysis was performed on the rotational speed and torque at peak power. Both correlate well with engine displacement for the two-stroke and

---

OS Engines, RCV Engines Ltd., Rotax Engines, Saito, Thunder Tiger, and Zenoah.

Table 2 Regression coefficients for power-law fits of engine mass as a function of engine total displacement, where m_{eng} is in kg and V_d in cm^3. 2S indicates two-stroke engines, while 4S stands for four-stroke

	A	B	R^2	R.U.
2S	0.1029	0.8667	0.9580	3.8%
4S	0.0532	0.9126	0.9893	3.5%

four-stroke engines (Figures 5 and 6). For both parameters a power-law fit was determined:

$$RPM_{peak} = AV_d^B \tag{8}$$
$$Q_{peak} = AV_d^B \tag{9}$$

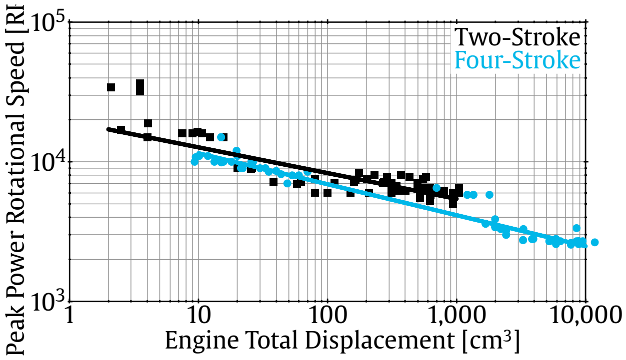

Fig. 5 Engine rotational speed at peak power as function of engine displacement.

The regression coefficients for rotational speed and torque are given in Tables 3 and 4 respectively. A good fit is obtained for both parameters with goodness-of-fit values above 0.9 for all but the regression for rotational speed for the two-stroke engine. The relative uncertainty values for both regressions are below 10% for the two engine types which makes the laws suitable for use in early design stages. Note that the three outliers for two-stroke engines of small displacement are not considered when determining the correlation but are included in the figures to indicate the spread on the data.

Table 3 Regression coefficients for power-law fits of engine rotational speed as function of engine displacement, where RPM_{peak} is in RPM and V_d in cm^3.

	A	B	R^2	R.U.
2S	19394	-0.1843	0.7892	5.2%
4S	19175	-0.2217	0.9349	7.6%

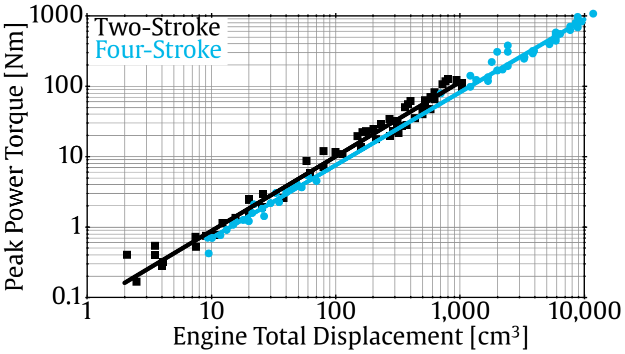

Fig. 6 Engine torque at peak power as function of engine displacement.

Table 4 Regression coefficients for power-law fits engine torque at peak power as function of engine displacement, where Q_{peak} is in Nm and V_d in cm^3.

	A	B	R^2	R.U.
2S	$7.732 \cdot 10^{-2}$	1.0571	0.9829	7.4%
4S	$6.425 \cdot 10^{-2}$	1.0355	0.9956	3.6%

3.1.3 Engine Efficiency

While data on engine power, displacement, mass, torque and rotational speed are readily available, efficiency is typically not given by manufacturers for all but the largest (general aviation) engines [40]. While efficiency generally decreases gradually when scaling down engines, it has furthermore been shown that a simple power law looses accuracy for engines with a displacement below 10 cm^3 [40]. The following modified power law is therefore adopted [40]:

$$\eta = \frac{AV_d^B \cdot \left(1 - CV_d^{-2/3}\right)}{100} \tag{10}$$

where η is the thermal efficiency of the engine at peak power, and A and B are the standard power-law regression coefficients. The additional regression coefficient C is introduced to account for the rapid decline in efficiency for small engines [40]. For engines with displacement larger than 10 cm^3, C is taken as zero while two values are proposed for smaller engines: 0.84 when the engine has a muffler, or 0.24 for engines without mufflers [40]. Note that those values are derived for glow engines.

In ref. [40] a value of 14.21 for A and a slope B of 0.08 is proposed for all engine types. For the current model 0.08 is retained for the slope B. However, for the proportionality constant A, a differentiation is made between the various engine types based on data from Rotax engines (Rotax 447, 503, 582, 912 UL, 912 ULS and 914) and measurements from refs. [42–47]. Nevertheless, separating engine classes is hard as scatter on engine efficiency is large, as was also noted in ref. [40]. To overcome this, the regression coefficient A is calibrated from the larger Rotax engines. Based on these calibrations a value of 12.21 is adopted for two-stroke engines, which matches well with data on 100 cm^3 engines from refs. [43, 47, 48]. For four-stroke engines, on the other hand, A is taken as 16.14 which is average value for the Rotax 912UL, 912ULS, and 914 engines. This value aligns with measured data for small (25 to 35 cm^3) Honda four-stroke engines [42, 44, 46]. The resulting fits are shown in Figure 7.

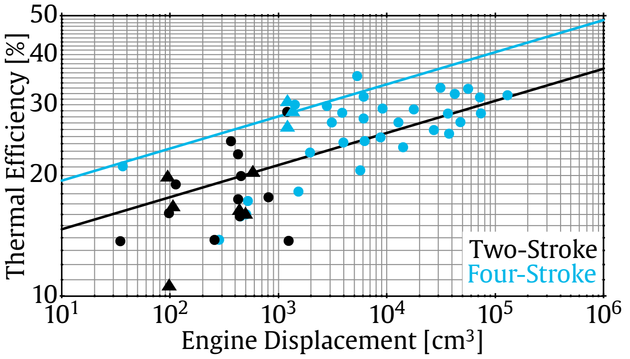

Fig. 7 Variation of efficiency at peak power with engine displacement. Data points from refs. [42–44, 46, 47] are indicated by triangles, while data points from ref. [40] are given by circles.

3.1.4 Engine Performance Maps

While the above correlations give values for efficiency at peak power, for mission calculations efficiency also needs to be known at other operating points. To determine engine efficiency at off-peak conditions, normalised efficiency maps are created based on data for a small two-stroke engine [49], and a 1.9 litre 95 kW four-stroke engine [50]. Map scaling is accomplished by normalising the rotational speed with the value at peak power, while torque is normalised by the wide-open throttle line and engine efficiency is scaled with the efficiency at peak power.

The following analytical expression is fitted to the normalised data [50, 51]:

$$\begin{aligned}\eta = {} & a_0 + a_1 x + a_2 y + a_3 xy + a_4 x^2 + a_5 y^2 + a_6 x^2 y \\ & + a_7 x \ln(x) + a_8 y \ln(y) + a_9 \ln(x) + a_{10} \ln(y),\end{aligned} \tag{11}$$

where a_0 through a_{10} are the fitting coefficients, x is the non-dimensionalised rotational speed, and y is the non-dimensionalised torque. The coefficients for the two maps are given in Table 5 and the resulting normalised efficiency maps are shown in Figures 8 and 9. R^2-values above 0.990 are obtained for the two-stroke map, while the four-stroke engine map was approximated with an R^2-value of 0.940.

As engine torque is non-dimensionalised by the wide-open throttle line, the torque at wide-open throttle is fitted with a fourth-order polynomial:

$$y = p_1 x^4 + p_2 x^3 + p_3 x^2 + p_4 x + p_5, \tag{12}$$

where p_1 through p_5 are the fitted coefficients, x is the non-dimensionalised rotational speed, and y is the non-dimensionalised torque at wide-open throttle. The coefficients of the polynomial are

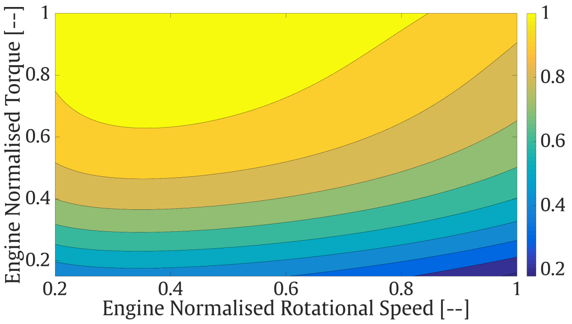

Fig. 8 Normalised efficiency map for two-stroke engines. Contour levels indicate normalised thermal efficiency, with normalisation performed using the thermal efficiency at peak power.

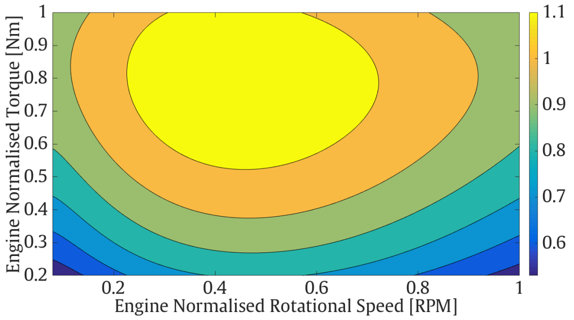

Fig. 9 Normalised efficiency map for four-stroke engines. Contour levels indicate normalised thermal efficiency, with normalisation performed using the thermal efficiency at peak power.

Table 5 Regression coefficients for the non-dimensionalised efficiency maps.

	2S	4S		2S	4S
a_0	-1.503	0.6824	a_6	2.931	0.5358
a_1	-1.002	0.717	a_7	0.1971	-3.66
a_2	-0.9827	0.8585	a_8	2.129	3.048
a_3	1.703	-0.6433	a_9	-6.341	-0.451
a_4	-0.06857	1.258	a_{10}	0.7024	0.7318
a_5	-1.324	-2.492			

given in Table 6. R^2-values above 0.995 are obtained for each WOT line.

The non-dimensionalised maps and wide-open throttle lines can be used in combination with the regression fits for RPM, torque, and efficiency at peak power (equations 8, 9 and 10) to create unscaled maps of engines of a different displacement.

Table 6 Regression coefficients for the non-dimensionalised wide-open throttle line.

	2S	4S
p_1	-3.423	-4.211
p_2	11.75	10.27
p_3	-15.38	-9.348
p_4	8.188	3.821
p_5	-0.1326	0.4742

3.2 Altitude Effects

As reciprocating engines use atmospheric air both the power output and efficiency of the engine are affected by the operating pressure. Altitude effects on power can be accounted for through the Gagg-Farrar correction [21, 37, 52]:

$$\phi(\sigma) = \frac{\sigma - D}{1 - D} \tag{13}$$

where D is 0.12 for typical piston engines [37], and σ represents the ratio of the air density at the considered altitude to the air density at sea level. Power at altitude is then given by:

$$P(\sigma) = \phi(\sigma) P_{SL} \tag{14}$$

and it is assumed that this correction factor applies equally across the entire engine map [21, 37, 52].

Brake specific fuel consumption (BSFC), or engine efficiency, is also corrected for altitude [21]:

$$F_{BSFC} = \frac{\sigma \cdot (1 - E)}{(\sigma^F - E)} \tag{15}$$

where E is 0.065 and F is 1.117 for large general aviation ICEs [21]. In the absence of detailed information, this altitude correction is assumed to apply to all engine types. Brake specific fuel consumption at altitude ($BSFC_{alt}$) is then given by:

$$BSFC_{alt} = F_{BSFC} BSFC_{SL} \tag{16}$$

where $BSFC_{SL}$ is the fuel consumption at sea-level.

3.3 Protom Exchange Membrane Fuel Cell Model

The current section describes the model used to size the proton exchange membrane (PEM) fuel cells. The weight and dimensions of the fuel cell are determined based on the required peak power of the fuel cell. Fuel cells need to be combined with brushless DC motors. Their performance is modeled here using the methodology described in ref. [34]. Variations in the zero-load current, motor armature resistance, and motor speed constant with continuous output power are modelled using correlations based on a regression analysis of 1743 outrunner motors from 12 manufacturers.

3.3.1 Fuel Cell Weight and Dimensions

Fuel cell sizes and weights have reduced considerably over the last decade due to major development programs in the automotive sector. As a consequence, current fuel cell technology has a comparable size and weight as internal combustion engines (ICE) as shown on Figure 10. The figure shows that automotive fuel cells are on par or even outperform ICE for both specific power and power density. For the investigations reported here a specific power of 2500 W/kg and a power density of 3.7 W/cm^3 are adopted for a 90 kW fuel cell.

The power density and specific power can then be used, in conjunction with the fuel cell peak power (which is derived from the mission under consideration), to determine the fuel cell dimensions. Before this can be done, however the number of cells in the stack needs to be determined first.

For large PEM fuel cells data is taken from [59, 60] to derive trends. For fuel cells ranging from 5 kW to 180 kW the number of cells scales almost linearly with output power. The following expression was therefore adopted:

$$N = 3 \cdot P_{\text{peak}} \tag{17}$$

Fuel cell stack height on the other hand is found to correlate well with the number of cells:

$$h_{\text{stack}} = 0.857 \cdot (N - 75) + 0.25 \tag{18}$$

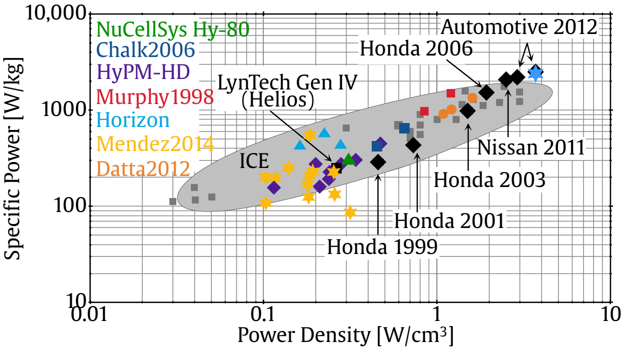

Fig. 10 Ragone plot to indicate progress in fuel cell technology (adapted from [53] with automotive data from [54, 55]). Additional data from [55–60] is added as indicated in the legend. Adopted value is indicated by the cyan star.

The cell area is on the other hand determined as function of the peak power to meet the specified power density. Fuel cell weight is calculated from the specified specific power. To account for scaling effects, the nominal power density and specific power are adjusted for fuel cell size based on trends identified in [59]. Adjustment factors are given in Table 7 where SPF stands for specific power factor and PDF denotes the power density factor. A linear interpolation between the values reported in Table 7 is used for intermediate powers [59].

Table 7 Adjustment Factors for Specific Power (SP) and Power Density

P_{peak} **[kW]**	**SPF**	**PDF**
10	0.833	0.7
30	0.815	0.808
90	1	1
150	1.158	1.167

3.3.2 Fuel Cell Efficiency

The efficiency of a PEM fuel cell will, in contrast to most reciprocating engines, improve at part load. In contrast to small fuel cells, efficiency for large fuel cells furthermore depends on the size (power) of the fuel cell. Large fuel cells namely typically employ a much more complicated balance-of-plant (BOP). While small fuel cells use fans to provide air, large fuel cells use compressors and operate at higher than ambient pressure. While this can improve fuel cell performance, the parasitic losses of the BOP will change with the nominal power of the fuel cell and the assumption of constant normalised efficiency no longer holds [59]. In the investigations presented in this report this is accounted for based on data from [59] as shown in Figure 11. For intermediate power levels, the efficiency curves are interpolated linearly [59].

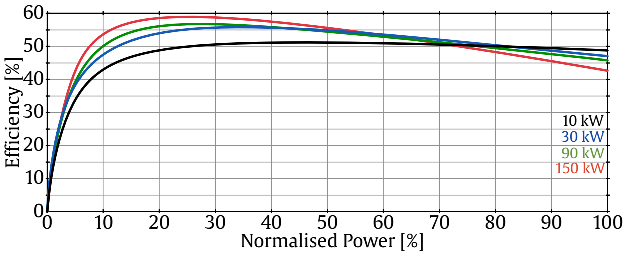

Fig. 11 Fuel Cell Efficiency in function of normalised power

With the fuel cell efficiency known, fuel consumption is determined based on the lower heating value (LHV) of hydrogen:

$$\dot{m}_F = \frac{P}{\eta_{FC} \cdot LHV} \tag{19}$$

where P is the power required from the fuel cell for the mission phase under consideration and η_{FC} is the fuel cell efficiency at the normalised power. The lower heating value for hydrogen is taken as 119.98 MJ/kg.

3.3.3 Altitude Effects

As fuel cells use ambient air to provide energy, their performance will change with altitude. While some investigations report changes in loss contributions and parasitic power requirements for the fuel cell BOP, only limited data is available on altitude effects [10–12, 61]. In general it is therefore assumed that fuel cell power varies with oxygen partial pressure as given by the Nernst equation [62]:

$$E = E_0 + \left(\frac{RT}{2F}\right) \cdot ln\left[\frac{P_{H_2}}{P_{H_2O}}\right] + \left(\frac{RT}{2F}\right) \cdot ln\left[P_{O_2}^{1/2}\right] \tag{20}$$

In the absence of more detailed data fuel cell power is therefore assumed to vary with the natural logarithm of the operating pressure.

3.4 Hydrogen Storage

While PEM fuel cells are more efficient and can, potentially, be lighter than incumbent technology, they operate on hydrogen. With a lower heating value of 119.98 MJ/kg hydrogen is much lighter than conventional aviation fuels. However hydrogen has a much lower density than conventional liquid fuels, even when stored at high pressure or as a (cryogenic) liquid. Hydrogen storage technology is thus key to the performance of fuel-cell-powered vehicles and aircraft as was demonstrated by the three-fold increase in endurance of the Spider-Lyon UAV when converting from compressed gaseous hydrogen (GH_2) to liquid hydrogen (LH_2) [63–65].

Hydrogen storage can broadly be divided into 3 categories [9]: compressed GH_2, chemical storage, and LH_2. As chemical storage has, to date, not been used for larger aviation applications, only the compressed gas and liquid hydrogen storage categories are considered here.

3.4.1 Hydrogen Storage Modelling

Both types of hydrogen storage have been modelled so that comparisons can be made. Rather than adopting a single gravimetric and volumetric density for each technology, the impact of storage capacity on the tank size and weight have been included. After all smaller tanks will tend to have much lower gravimetric and volumetric densities than tanks containing a considerable amount of hydrogen. To include these effects both gravimetric and volumetric density are varied with the natural logarithm of the stored hydrogen quantity.

The gravimetric and volumetric densities for the considered storage technologies are shown on Figure 12. For each technology the hydrogen quantities used to determine the lines on the Figure are included between brackets. They roughly indicate the applicability of the technology. A tank length-to-diameter ratio of 3 is assumed for all tanks in this investigation.

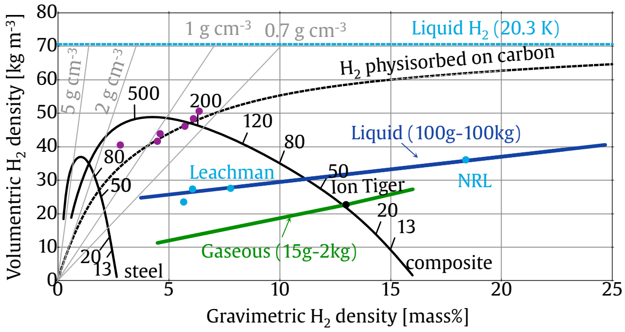

Fig. 12 Adopted models for the different storage technologies (adapted from [66] with additional data from [9, 67, 68])

As fuel cells require the use of brushless DC

4 Results

MALE UAVs have widely varying quoted times on-station. Endurances range from 6 hours for smaller platforms to 24-40 hours for larger scale MALE UAVs. For the investigations in this work time-on-station was thus varied from 6 to 70 hours so that a large range of platform sizes can be explored and differences between propulsion technologies become more apparent. For each technology and endurance value, the wing area and wing platform are optimised so that the aircraft with minimal take-off gross weight is found. Optimisation is initiated using a latin hypercube design with a population size of 45 and is evolved over 5 generations with the MATLAB® in-built particle swarm optimisation algorithm. A population based algorithm is used to initiate the optimisation to ensure that a global minimum is found rather than a local minimum. Once the 5 generations are computed, the solution is further refined using the MATLAB® gradient-based `fmincon` algorithm. Constraints are applied to ensure that a sufficient margin is obtained over the stall speed of the aircraft and to restrict operation to reasonable Reynolds numbers [6].

The baseline MALE UAV is sized to house a payload of 100 kg that draws 1500 W of power. This is a typical operational payload of a Predator A mission [21] and allows to carry both EO/IR and a full SAR payload. For instance, a Versatron Skyball EO/IR with supporting electronics and a Lynx SAR payload have a combine weight of 82.1 kg [21]. Results of this investigation are given in Figures 13 to 14.

Figure 13 shows that the weight of the platforms that use an internal combustion engine rises much more rapidly than that of those who are powered by fuel cells. For the comparatively large fuel weights of those platforms the weight reduction due to the much higher LHV of hydrogen more than compensates the increase in tank mass. Take-off weights around 1500 kg are reached for an endurance around 30 to 40 hours for the piston engine powered vehicles. For fuel-cell powered vehicles, on the other hand, take-off gross weight is about half this value at this endurance. Even for a much larger endurance the MTOW of the MALE UAV with PEM fuel cells does not exceed 1000 kg. As the hydrogen storage capacity of the tanks becomes significant, liquid hydrogen storage shows a significant advantage over gaseous compressed storage. Even for a loiter endurance of 70 hours, the maximum take-off weight with liquid hydrogen only reaches 560 kg.

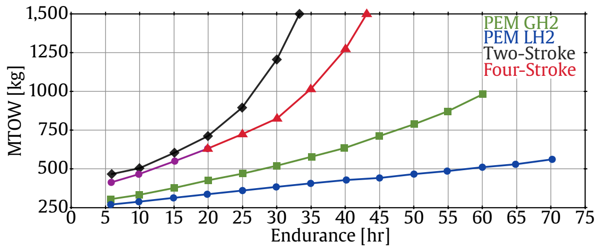

Fig. 13 Take-Off Weight for the MALE UAV category

Figure 14 shows that the large reduction in fuel mass also influences the empty weight of the vehicle. The empty weight of the MALE

UAVs which use fuel cells is lower than that of the piston-powered vehicles. A large part of the vehicle empty weight is namely influenced by the take-off weight. Wing weight, for instance, increases with wing area and the drastic reduction in fuel weight (and take-off weight) leads to a much smaller wing area. Wing loadings for all considered propulsion systems are namely very similar (around 90-95 kg/m^2). Similar observations can be made for the weights of the other components of the airframe.

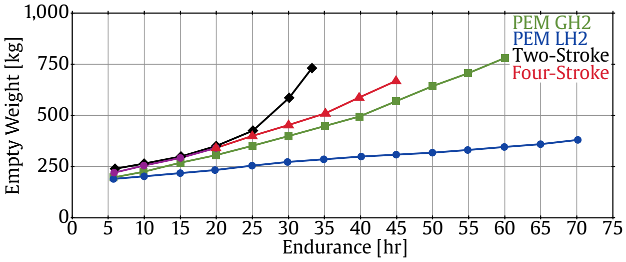

Fig. 14 Empty Weight for the MALE UAV category

The significant impact of the fuel weight also influences the size of the engine / motor, as shown on Figure 15. The overall reduction in take-off weight more than compensates the more rapid loss of power with altitude for the fuel cells, and a much smaller motor is required for the fuel cell vehicles. Despite the lower engine power, the power-to-weight ratio for the fuel-cell-powered vehicles increased to around 150-160 W per kg of MTOW. The UAVs with internal combustion engines, on the other hand, have a power-to-weight ratio that varies from 130 W/kg at low endurances down to 100 W/kg at the highest considered endurance.

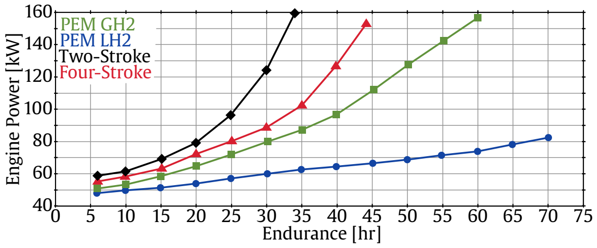

Fig. 15 Engine Power for the MALE UAV category

The impact of payload weight was also investigated for MALE UAVs. After all, this category has a wide range of advertised payload capabilities. The baseline payload weight was doubled to 200 kg and the required payload power was increased accordingly (to 3000 W). Results of this investigation are shown in Figure 16. Figure 16 shows that the increased payload weight has a strong influence on the overall maximum take-off mass, especially for the vehicles with internal combustion engines. The endurance at a take-off gross weight of 1500 kg decreases by 10 to 15 hours for all internal combustion engines. The impact on the fuel-cell powered vehicle with compressed gas storage is equally significant. While the take-off gross weight of the UAVs with liquid hydrogen storage also increases, the MTOW still stays within bounds even at 70 hours endurance.

The increase in MTOW has a significant impact on the required engine power. At low endurances engine power increases from 50 kW to approximately 80 kW. At an endurance of 70 hours, the fuel cell powered vehicle requires a motor with approximately 140 kW of power, while the MALE UAV with the smaller payload only required 80 kW.

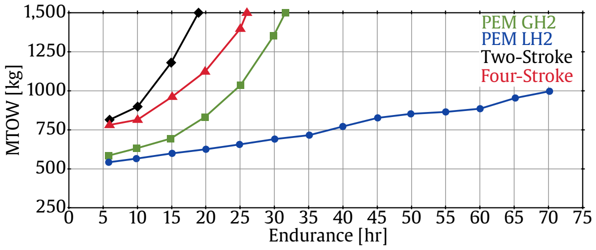

Fig. 16 Take-Off Weight for the MALE UAV category with Larger Payload

5 Conclusion

The current article presents a multidisciplinary design and optimisation framework that allows a comparison between piston engines and fuel cells as a propulsion system for medium altitude long endurance UAVs. While medium altitude long endurance unmanned vehicles are typically powered by piston engines, it is shown that fuel cells can offer significantly higher endurance. For a given take-off weight the use of fuel cells almost doubles the endurance of the UAV and endurances well over 60 hours are achievable with take-off gross weights less than 1000 kg. While compressed gaseous hydrogen storage offers weight reductions compared to piston engines, liquid hydrogen allows for much more significant weight reductions especially for larger payload weights.

References

[1] O. Gur, A. Rosen, Optimizing electric propulsion systems for unmanned aerial vehicles, Journal of Aircraft 46 (4) (2009) 1340–1353.

[2] K. Kim, T. Kim, K. Lee, S. Kwon, Fuel cell systems with sodium borohydride as hydrogen source for unmanned aerial vehicles, Journal of Power Sources 196 (2011) 9069–9075.

[3] D. Verstraete, K. Lehmkuehler, A. Gong, J. Harvey, G. Brian, J. Palmer, Characterisation of a hybrid, fuel-cell-based propulsion system for small unmanned aircraft, Journal of Power Sources 250 (2014) 204–211.

[4] D. Verstraete, A. Gong, D.-C. Lu, J. Palmer, Experimental investigation of the role of the battery in the aerostack hybrid, fuel-cell-based propulsion system for small unmanned aircraft systems, International Journal of Hydrogen Energy 40 (2015) 1598–1606.

[5] A. Gong, J. L. Palmer, G. Brian, J. R. Harvey, D. Verstraete, Performance of a hybrid, fuel-cell-based power system during simulated small unmanned aircraft missions, International Journal of Hydrogen Energy 41 (26) (2016) 11418–11426.

[6] D. Verstraete, L. Cazzato, G. Romeo, Preliminary design of a fuel-cell-based hybrid-electrical uav, in: 28th International Congress of the Aeronautical Sciences, Vol. 1, ICAS-2012-654, 2012, pp. 422–431.

[7] A. Gong, D. Verstraete, Fuel cell propulsion in small fixed-wing unmanned aerial vehicles: Current status and research needs, International Journal of Hydrogen Energy 42 (33) (2017) 21311 – 21333.

[8] C. Riboldi, F. Gualdoni, An integrated approach to the preliminary weight sizing of small electric aircraft, Aerospace Science and Technology 58 (2016) 134–149.

[9] A. Gong, D. Verstraete, Fuel cell propulsion in small fixed-wing unmanned aerial vehicles: Current status and research needs, International Journal of Hydrogen Energy 42 (33) (2017) 21311–21333.

[10] J. Pratt, J. Brouwer, G. Samuelsen, Experimental performance of an air-breathing pem fuel cell at high altitude conditions, in: 43rd AIAA Aerospace Sciences Meeting and Exhibit, Aerospace Sciences Meetings, American Institute of Aeronautics and Astronautics, 2005.

[11] J. Pratt, J. Brouwer, G. Samuelsen, Performance of proton exchange membrane fuel cell at high-altitude conditions, J. Propul. Power 23 (2) (2007) 437–444.

[12] T. Hordé, P. Achard, R. Metkemeijer, Pemfc application for aviation: Experimental and numerical study of sensitivity to altitude, Int. J. Hydrogen Energy 37 (14) (2012) 10818–10829.

[13] D. Verstraete, J. Palmer, M. Hornung, Preliminary sizing correlations for fixed-wing uav characteristics, Journal of Aircraft 55 (2) (2018) 715–726.

[14] R. Austin, Unmanned Aircraft Systems: UAVS Design, Development and Deployment, Aerospace Series, Wiley, 2010.

[15] NATO, Fuel Cells and Other Emerging Manportable Power Technologies for the NATO Warfighter – Part II: Power Sources for Unmanned Applications, no. STO-TR-SET-173, NATO Science and Technology Organization, 2014.

[16] R. Fink, Usaf stability and control datcom, Tech. rep., AFWAL-TR-83-3048, McDonnell Douglas Corporation, Douglas Aircraft Division, for the Flight Controls Division, Air Force Flight Dynamics Laboratory, Wright-Patterson AFB (1978).

[17] USAF, The usaf stability and control digital datcom, volume i, users manual., Tech. rep., USAF Technical report AFFDL-TR-79-3032 (1979).

[18] J. Gundlach, Designing Unmanned Aircraft Systems: A Comprehensive Approach, AIAA Education Series, AIAA, New York, 2011.

[19] T. Nam, D. Soban, D. Mavris, A Generalized Aircraft Sizing Method and Application to Electric Aircraft, American Institute of Aeronautics and Astronautics, 2005.

[20] J. S. Parsons, R. E. Goodson, The optimum shaping of axisymmetric bodies for minimum drag in incompressible flow, Tech. rep., Purdue University (1972).

[21] J. Gundlach, Multi-disciplinary design optimization of subsonic fixed-wing unmanned aeroial vehicles projected through 2025, Ph.D. thesis, Virginia Polytechnic Institue and State University (2004).

[22] D. Raymer, Aircraft Design: A Conceptual Approach, 4th Edition, AIAA Education Series, AIAA, New York, 2006.

[23] J. Roskam, Airplane Design Parts I-VIII, DARcorporation, 1997.

[24] L. M. Nicolai, G. Carichner, Fundamentals of Aircraft and Airship Design: Volume 1 Aircraft Design, AIAA Education Series, AIAA, 2010.

[25] H. Chevalier, Model Airplane Design and Performance for the Modeler, Challenge Engineering, New Baden, TX, 1993.

[26] C. L. Needham, Sailplanes Their Design, Construction and Pilotage, Chapman and Hall Ltd., 1937.

[27] F. Thomas, Fundamentals of Sailplane Design, College Park Press, 1999.

[28] J. Gundlach, R. J. Foch, Unmanned Aircraft Systems Innovation at the Naval Research Laboratory, Library of Flight, American Institute of Aeronautics and Astronautics, Reston , VA, 2014. `doi:10.2514/4.102592`.

[29] A. Chaput, Conceptual design of unmanned aircraft systems, Tech. rep., Kansas University Continuing Education (2007).

[30] S. Gudmundsson, General Aviation Aircraft Design: Applied Methods and Procedures, Elsevier, Waltham, MA, 2014.

[31] Z. Yi, W. Heping, A study of structure weight estimating for high altitude long endurence (hale) unmanned aerial vehicle (uav), in: 25^{th} International Congress of the Aeronautical Sciences, Hamburg, Germany, 2006.

[32] M. Bailey, M. Bower, High altitude solar power platform, Tech. rep., NASA-TM-103578 (1992).

[33] C. Roessler, Conceptual design of unmanned aircraft with fuel cell propulsion system, Ph.D. thesis, Lehrstuhl fuer Luftfahrtsysteme, Technical University Munich (2012).

[34] R. MacNeill, D. Verstraete, Propeller optimisation for an electrically-powered tactical uas, in: Proceedings of the 31^{st} Congress of the International Council of the Aeronautical Sciences, Belo Horizonte, Brasil, 2018.

[35] A. Noth, Design of solar powered airplanes for continuous flight, Ph.D. thesis, ETH Zurich (2008).

[36] M. McCrink, J. W. Gregory, Range and Endurance Estimation for Low-Re Electric UAS, American Institute of Aeronautics and Astronautics, 2017.

[37] J. T. Lowry, Performance of Light Aircraft, AIAA Education Series, AIAA, 1999.

[38] Selig. Uiuc propeller database [online] (2016) [cited June 2016].

[39] M. Simons, Model Aircraft Aerodynamics, 4th Edition, Special Interest Model Books, 1999.

[40] S. Menon, C. P. Cadou, Scaling of miniature piston-engine performance, part 1: Overall engine performance, Journal of Propulsion and Power 29 (4) (2013) 774–787.

[41] E. Sher, I. Sher, Theoretical limits of scaling-down internal combustion engines, Chemical Engineering Science 66 (3) (2011) 260 – 267.

[42] J. K. Ausserer, Integration, testing, and validation of small hybrid-electric remotely-piloted aircraft, Master's thesis, Air Force Institute of Technology (2012).

[43] S. C. Crosbie, Increasing reliability of a small 2-stroke internal combustion engine for dynamically changing altitudes, Master's thesis, Air Force Institute of Technology (2012).

[44] F. G. Harmon, Neural network control of a parallel hybrid-electric propulsion system for a small unmanned aerial vehicle, Ph.D. thesis, University of California, Davis (2005).

[45] R. M. Hiserote, Analysis of hybrid-electric propulsion system designs for small unmanned aircraft systems, Master's thesis, Air Force Institute of Technology (2010).

[46] I. H. Mengistu, Small internal combustion engine testing for a hybrid-electric remotely-piloted aircraft, Master's thesis, Air Force Institute of Technology (2011).

[47] N. L. Moulton, Performance measurement and simulation of a small internal combustion engine, Master's thesis, University of Maryland (2007).

[48] A. Ravi, A. S. Arena, Uav power plant performance evaluation, in: Proceedings of the 49^{th} AIAA Aerospace Sciences Meeting including the New Horizons Forum and Aerospace Exposition, no. AIAA-2011-1263, 2011.

[49] S. P. Hendrickson, A miniature powerplant for very small, very long range autonomous aircraft, Tech. rep., The Insitu Group, Final Report to the United States Department of Energy (1999).

[50] K. B. Wipke, M. R. Cuddy, S. D. Burch, Advisor 2.1: a user-friendly advanced powertrain simulation using a combined backward/forward approach, IEEE Transactions on Vehicular Technology 48 (6) (1999) 1751–1761.

[51] T. Markel, A. Brooker, T. Hendricks, V. Johnson, K. Kelly, B. Kramer, M. O'Keefe, S. Sprik, K. Wipke, Advisor: a systems analysis tool for advanced vehicle modeling, Journal of Power Sources 110 (2) (2002) 255 – 266.

[52] D. Stinton, The Design of the Aeroplane, 2nd Edition, Blackwell Scientific, 2001.

[53] E. D. Wachsman, K. T. Lee, Lowering the temperature of solid oxide fuel cells, Science 334 (2011) 935–939.

[54] Oak Ridge National Laboratory, Status and Prospects of the Global Automotive Fuel Cell Industry and Plans for Deployment of Fuel Cell Vehicles and Hydrogen Refueling Infrastructure.

[55] T. Lukaczyk, A. D. Wendor, E. Botero, T. MacDonald, T. Momose, A. Variyar, J. M. Vegh, M. Colonno, T. D. Economon, J. J. Alonso, Suave: An open-source environment for multi-fidelity conceptual vehicle design, in: Proceedings of the 16^{th} AIAA/ISSME Multidisciplinary Analysis and Optimization Conference, no. AIAA-2015-3087, 2015.

[56] O. J. Murphy, A. Cisar, E. Clarke, Low-cost light weight high power density pem fuel cell stack, Electrochimica Acta 43 (24) (1998) 3829–3840.

[57] S. G. Chalk, J. F. Miller, Key challenges and recent progress in batteries, fuel cells, and hydrogen storage for clean energy systems, Journal of Power Sources 159 (2006) 73–80.

[58] Horizon Energy Systems. Horizon Energy Systems Aeropak Specifications [online] (2016) [cited February 2016].

[59] I. L. Sarioglu, B. Czapnik, E. Bostanci, O. P. Klein, H. Schroeder, F. Kucukay, Optimum design of a fuel-cell powertrain based on multiple design criteria, Journal of Power Sources 266 (2014) 7–21.

[60] Hydrogenics, Hypm-hd power modules for light and heavy duty mobility, Tech. rep., Hydrogenics (2016).

[61] V. Chang, J. Gallman, Altitude testing of fuel cell systems for aircraft applications, in: Proceedings of the Power Systems Conference, SAE Technical Paper 2004-01-3200, SAE Technical Paper 2004-01-3200, 2004.

[62] J. Larminie, A. Dicks, Fuel Cell Systems Explained, 2nd Edition, Wiley, 2003.

[63] R. Stroman, M. Schuette, Design challenges and modeling for an efficient liquid hydrogen storage tank for autonomous systems, 11AIChE - 2011 AIChE Annual Meeting, Conference Proceedings.

[64] K. Swider-Lyons, J. Mackrell, J. Rodgers, G. Page, M. Schuette, R. Stroman, Hydrogen fuel cell propulsion for long endurance small UAVs, AIAA Centennial of Naval Aviation Forum "100 Years of Achievement and Progress".

[65] K. Swider-Lyons, R. Stroman, J. Rodgers, D. Edwards, J. Mackrell, M. Schuette, G. Page, Liquid hydrogen fuel system for small unmanned air vehicles, 51st AIAA Aerospace Sciences Meeting including the New Horizons Forum and Aerospace Exposition 2013.

[66] A. Züttel, Hydrogen storage methods, Naturwissenschaften 91 (4) (2004) 157–172.

[67] R. O. Stroman, M. W. Schuette, K. Swider-Lyons, J. A. Rodgers, D. J. Edwards, Liquid hydrogen fuel system design and demonstration in a small long endurance air vehicle, International Journal of Hydrogen Energy 39 (21) (2014) 11279–11290.

[68] P. Adam, J. Leachman, Design of a reconfigurable liquid hydrogen fuel tank for use in the Genii unmanned aerial vehicle, Transactions of the Cryogenic Engineering Conference-CEC: Advances in Cryogenic Engineering 1573 (1) (2014) 1299–1304.

Contact Author Email Address

dries.verstraete@sydney.edu.au

Copyright Statement